

Pb(II) Adsorption on Isostructural Hydrated Alumina and Hematite (0001) Surfaces: A DFT Study[†]

Sara E. Mason,[‡] Christopher R. Iceman,[§] Kunaljeet S. Tanwar,[§] Thomas P. Trainor,[§] and Anne M. Chaka^{*‡}

Physics Laboratory, National Institute of Standards and Technology, Gaithersburg, Maryland 20899, and Department of Chemistry and Biochemistry University of Alaska, Fairbanks, P.O. Box 756160, Fairbanks, Alaska 99775

Received: August 15, 2008; Revised Manuscript Received: December 22, 2008

The persistence of lead (Pb) in contaminated topsoil is ranked as one of the most serious environmental issues in the U.S. and other countries. Adsorption of Pb at the aqueous interface of nanoscale metal oxide and metal (oxy)hydroxide particles is perhaps the most significant process responsible for controlling contaminant sequestration and mobility, but the process is poorly understood at the molecular level. Experimental studies of absorption of Pb onto bulk minerals have indicated significant differences in reactivity, but the molecular basis for these differences has remained elusive due to the challenges of observing and modeling the complex chemistry that exists at the water–oxide interface. In this work, we present a detailed ab initio theoretical investigation aimed at understanding the fundamental physical and chemical characteristics of Pb adsorption onto the (0001) surface of two common minerals, α -Al₂O₃ and α -Fe₂O₃. The results of our periodic density functional theory (DFT) calculations show that the adsorption energy of Pb(II) on hematite is more than four times the value on isostructural alumina with the same fully hydroxylated surface stoichiometry due to bonding interactions enabled by the partially occupied Fe d-band. Site preference for Pb(II) adsorption on alumina is shown to depend strongly on the cost to disrupt highly stable hydrogen bonding networks on the hydrated surface, but is less of a factor for the stronger Pb-hematite interaction.

I. Introduction

Lead (Pb) contamination is ranked as one of the most serious environmental issues by the Environmental Protection Agency and the U.S. Department of Health and Human Services' Agency for Toxic Substances and Disease Registry, with significant consequences for human health and bioaccumulation in ecosystems.¹ At relatively low levels in the blood (no safe blood level of Pb in children has been determined), Pb is toxic to nearly every organ in the body and is particularly problematic for neurological development, the hematological and cardiovascular systems, and the kidney. Over the past three hundred years, environmental levels of Pb have increased dramatically due to human activity, with the vast majority of anthropogenic Pb ultimately being dispersed in soils. Primary sources of Pb contamination include car exhaust, fossil fuel and waste combustion, pesticides applied to fruit orchards prior to 1950, wastewater from iron and steel manufacturing, battery manufacture, and weathering and chipping of Pb paint from homes, buildings, and bridges. Vehicle exhaust in the U.S. resulted in the release of 943 925.7 metric tons of Pb in 1979 alone. Despite recent restrictions on the use of Pb in gasoline and paints in some countries such as the United States, contamination remains a serious issue. Pb is also commonly associated with sulfide mineral deposits and is a contaminant of concern associated with mineral resource development.² Understanding why Pb persists in topsoil, i.e., how Pb binds to mineral surfaces in the

soil, and the conditions under which it is released and becomes bioavailable, is of considerable importance for hazard assessment and remediation strategies.

Within soils and sediments, Pb(II) generally partitions strongly to the solid phase, both limiting dissolved concentrations in aqueous systems, and resulting in persistence of contamination in the near surface environment.³ Among the possible modes of solid phase partitioning, adsorption of metal-ion contaminants at the aqueous interface of nanoscale metal oxide and metal (oxy)hydroxide particles is perhaps the most significant process responsible for controlling contaminant sequestration and mobility, and finds widespread use in remediation technologies.^{4,5} The reactivity of metal-(hydr)oxide phases stems from both the abundant surface area and the nature of the surface functional groups exposed to aqueous solution, generally consisting of hydroxyl moieties that can act as ligands for direct complexation of Lewis acids, Lewis base exchange sites, or sites for physical adsorption through Coulomb and hydrogen bonding (H-bonding) interactions.^{5,6} It is well known that the chemical characteristics of a mineral surface are a key factor in determining the strength of metal-ion partitioning and, therefore, the extent and stability of sorbed species.^{7,8} However, developing a molecular level structure–reactivity relationship for mineral–sorbate interactions has been impaired by the experimental and theoretical challenges presented by the complex nature of these variable composition, heterogeneous systems. For instance, the interaction of water with oxide surfaces dictates the coordination chemistry of surface functional groups and, therefore, dictates reactivity in aqueous systems. The resulting surface structure and stoichiometry will typically be substantially different from that observed for nonhydroxylated clean surfaces, which are generally accessible to study by

[†] Part of the special section "Physical Chemistry of Environmental Interfaces".

* To whom correspondence should be addressed. E-mail: anne.chaka@nist.gov.

[‡] National Institute of Standards and Technology.

[§] University of Alaska, Fairbanks.

traditional ultrahigh vacuum (UHV) surface science methods.^{9–12} In fact, the presence of water leads to a variety of plausible chemical terminations, including variation in protonation states of surface (hydr)oxo groups, which must be considered in a molecular analysis of interface reactivity under environmental conditions.¹³

In this work, we present a detailed *ab initio* theoretical investigation aimed at understanding the fundamental structure–reactivity relationship of Pb adsorption in a model mineral–water interface system. Our study focuses on Pb(II) adsorbed to the hydroxylated (0001) surface termination of α -Al₂O₃ and α -Fe₂O₃. This work follows on numerous experimental investigations of Pb(II) adsorption onto iron and aluminum oxides and oxy(hydroxides),^{14–18} which are the focus of this study because of their high natural abundance and their large reactive surface areas in soil and sediment systems.^{19–22} Macroscopic studies of the partitioning of Pb(II) onto high surface area powders of iron and aluminum oxides have revealed a significant difference in the reactivity of these substrates, where in general uptake is stronger on the iron-bearing phases.^{22–27} Pb L-edge X-ray absorption spectroscopy (XAS) studies of powder systems have revealed that Pb(II) tends to bind in an inner-sphere manner based on observed Pb–O and Pb–Fe(Al) distances.^{3,28–30} More detailed analysis regarding the intrinsic differences in substrate reactivity are difficult to gain from studies utilizing powdered substrates since they do not provide direct information as to which crystal faces or surface functional groups are the predominant binding sites.

XAS studies utilizing oriented single crystals in a grazing-incidence geometry (GI-XAS) have been used to provide surface specific information regarding Pb(II) binding geometry and partitioning information. The GI-XAS study of Bargar et al.³¹ found that Pb(II) forms dominantly outer-sphere complexes at the α -Al₂O₃ (0001)/aqueous solution interface based on observation of a Pb–O distance of 2.51 (± 0.02) Å (the errors values resulting from the least-squares standard deviations), which is consistent with Pb(II) bonded to water molecules, and a Pb–Al distance of 5.78 (± 0.04) Å. If Pb(II) were bonded to oxo ligands, the Pb–O distance would fall in the range of 2.20 Å to 2.31 Å, whereas if bonded to hydroxo ligands, the Pb–OH distance would be 2.25 Å to 2.32 Å.³⁰ This result contrasted the observation of dominantly inner-sphere complexes on the α -Al₂O₃ (1 $\bar{1}$ 02) surface but was in agreement with the estimated differences in reactivity based on *ex situ* XPS measurements that show significantly greater uptake on the (1 $\bar{1}$ 02) surface.³¹

Studies of Pb binding on α -Fe₂O₃ (0001) and (1 $\bar{1}$ 02) surfaces indicate that Pb(II) forms dominantly inner-sphere complexes on both surfaces, with the (0001) surface having a higher coverage of Pb(II) than the (1 $\bar{1}$ 02) surface based on XPS results.³² These studies also indicate that the Fe₂O₃ surfaces are more reactive than the isostructural α -Al₂O₃ analogs. The partitioning behavior of Pb(II) to Al₂O₃ and Fe₂O₃ single crystal substrates has been investigated further in several long-period X-ray standing wave studies of Pb(II) partitioning.^{33–35} The summary of these experimental studies indicates that the Pb(II) reactivity sequence is as follows: α -Fe₂O₃ (0001) > α -Al₂O₃ (1 $\bar{1}$ 02) \approx α -Fe₂O₃ (1 $\bar{1}$ 02) \gg α -Al₂O₃ (0001).⁸ This reactivity trend is presumably associated with the differences in surface structures of these substrates, resulting in differences in Pb(II) binding modes, as well as the intrinsic reactivity differences due to the difference in composition and electronic properties of the materials.^{8,31–34,36} The major focus of the present study is to investigate this latter point: for a given surface structure, how do the differences in composition, and hence electronic

structure of the substrates, influence differences in sorption affinity for Pb(II)? In addition, we also examine the effect of hydroxylation and hydrogen-bonding on Pb adsorption structures and energies, as this information is not accessible using experimental techniques. We address these questions using density functional theory (DFT) methods to study inner-sphere binding of Pb(II) on structurally equivalent hydroxylated (0001) surfaces of α -Al₂O₃ and α -Fe₂O₃.

A. α -M₂O₃ (0001) Surface Structure. The alumina and hematite (0001) surfaces are stable terminations, and hence prevalent growth faces. Their interfaces with water have been widely investigated from both an experimental and theoretical perspective.^{37–41} In the bulk corundum structure, there are three unique cleavage planes to terminate the bulk to form a clean (0001) surface: a single metal ion (Fe or Al, labeled “M”) layer, a double metal ion layer, or an oxygen layer, as indicated in the following notation: M–O₃–M–R, M–M–O₃–R, and O₃–M–M–R, where R represents the continuing bulk atomic stacking sequence. Under UHV conditions, the experimental and theoretical evidence is consistent with a highly relaxed metal-terminated surface, M–O₃–M–R, for both α -Fe₂O₃^{42–45} and α -Al₂O₃^{46–55} This is the most stable surface from a stoichiometric and electrostatic perspective, as the polar oxygen anion layer is stabilized by an equal number of positive metal cations above and below.^{46,56} Exposing the clean Fe–O₃–Fe–R surface to high oxygen partial pressures (p_{O_2}) results in formation of two distinct chemical domains.^{44,57–60} Recent experimental and theoretical studies provide strong evidence for the formation of an oxygen-terminated ferryl (Fe=O) domain from a reaction of O₂ with the exposed surface Fe cation. The ferryl domain is shown to be more thermodynamically stable than the O₃–Fe–O₃–R terminated surface previously proposed by Wang et al.⁴⁴ at high oxygen partial pressures.^{59,61–63} The presence of the stable ferryl Fe=O functionality was shown by Jarvis and Chaka to be due to the formation of strong covalent bonds between the Fe 3d orbitals and the oxygen 2p orbitals.⁶¹ They also predicted that aluminum atoms on the clean Al–O₃–Al–R terminated surface are incapable of forming a stable Al=O interaction due to the lack of covalent overlap of aluminum’s high energy empty 3d orbitals with the oxygen 2p. The high surface free energy calculated by *ab initio* thermodynamics^{48,64,65} predicts that the electrostatic interactions between the aluminum cation and oxygen anion are not sufficient to stabilize an Al=O termination.

Exposure of the (0001) surface to water results in a complex range of possible hydroxylated structures. Exposure of the stoichiometric Fe–O₃–Fe–R terminated surface to increasing partial pressure of water vapor yields a fully hydroxylated surface³⁷ consistent with a (HO)_x–Fe–O₃–Fe–R structure that may persist at high $p_{\text{H}_2\text{O}}$.^{40,66–68} However, an analogous (HO)_x–Al–O₃–Al–R surface termination has not been experimentally observed on α -Al₂O₃. This stark contrast in stable surface structure compared to hematite has been offered as a possible explanation for the varying affinity of Pb(II) for these surfaces.⁶⁹ Experimental^{9,70} as well as theoretical^{48–50} evidence support the formation of a (HO)₃–Al–Al–R termination where the surface Al cation has been removed. Partial removal of the (0001) surface Fe cation has been observed to occur for hematite under conditions more relevant to environment exposure, i.e., exposure to liquid water rather than water vapor in a vacuum chamber.⁶⁹ A crystal truncation rod investigation of hematite (0001) surface structure that had been acid washed and rinsed with water revealed two surface domains.⁶⁹ Comparison of measured relaxations with the calculated DFT results

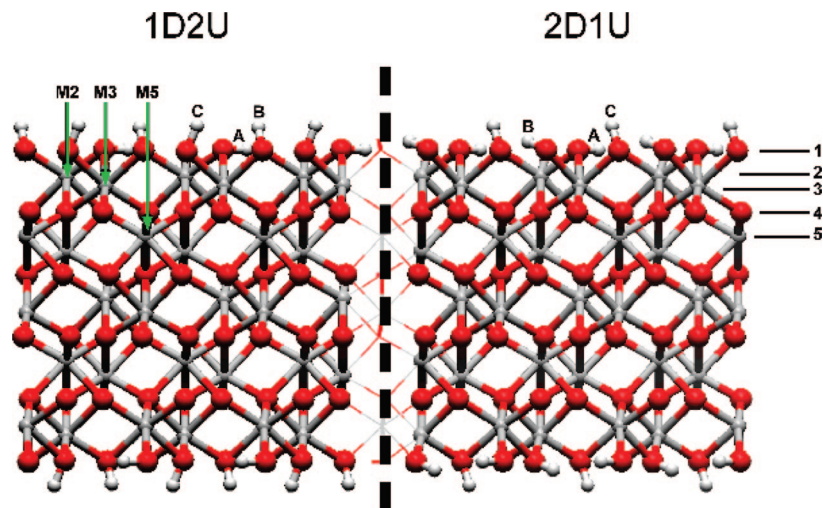


Figure 1. Side views of the oxygen terminated (0001) α - M_2O_3 surfaces with the “one down two up” (1D2U, left) and “two down one up” (2D1U, right) H-bond networks. The cations which define the centers of the M2, M3, and M5 adsorption sites, and the numeric atomic layers, (both labeling schemes invariant to H-bonding), are indicated on the 1D2U by vertical green lines and 2D1U panels by horizontal black lines, respectively. Oxygen atoms are shown as large red spheres, cations (Al or Fe) are shown by smaller gray spheres, and H^+ are shown in white.

indicated the dominant domain (60–62%) consisted of the $(HO)_3-Fe-Fe-R$ structure in which the surface Fe-cation had been removed. The remaining structure was consistent with the $(HO)_x-Fe-O_3-Fe-R$ termination observed by introducing water vapor to a clean $Fe-O_3-Fe-R$ terminated surface in a vacuum chamber.

The $(HO)_3-M-M-R$ termination is the dominant structure for the α - Fe_2O_3 (0001) surface, and the only one observed for α - Al_2O_3 under realistic conditions for the mineral–water interface. Through study of this common structural phase, we isolate and probe the relationship between composition and reactivity using this surface stoichiometry.

II. Methodology and Computational Details

DFT with the generalized gradient approximation (GGA) exchange correlation functional (XC) is well known to accurately describe the bulk and surface structures and energies of α - Al_2O_3 ,^{46,48,71,72} and α - Fe_2O_3 ,^{13,44,63,69} as well as the correct antiferromagnetic ground-state of hematite.⁷³ In this study we perform all-electron, spin-polarized (as necessary for modeling hematite) periodic DFT calculations, using a double-numeric-plus-polarization, atom-centered basis set and the GGA XC of Perdew, Burke, and Ernzerhof (PBE)⁷⁴ as implemented in the DMol³ code.^{75,76,96} Lattice optimizations were converged with respect to k -points using a Monkhorst-Pack (MP) grid⁷⁷ to sample the Brillouin zone, and a 4.5 Å real space cutoff (r_{cut} , reduced to 3.5 Å in subsequent surface and Pb adsorption calculations). The optimized lattice constants of 4.823 Å (+1.3%) and 13.111 Å (+0.9%) for α - Al_2O_3 and 5.044 Å (+0.1%) and 13.896 Å (+0.9%) for α - Fe_2O_3 are in excellent agreement with experiment (differences from experiment are indicated in parentheses),^{78,79} and other GGA results.^{13,44,46,48,63,69,71,72}

The hydrated α - Al_2O_3 and α - Fe_2O_3 (0001) surfaces are modeled using three-dimensional periodic slabs consisting of six O layers and 10 M layers, with an excess of 25 Å of vacuum between them. The top and bottom surfaces, related by inversion, are both completely hydroxylated, with one proton attached to every surface oxygen to form a nonpolar (charge neutral) surface consistent with previous work.^{48,69} The layers in the slab are referred to by numerical order beginning at the topmost layer, as shown in Figure 1. Full geometry optimization is carried out with no imposed symmetry on the entire slab, with structural convergence set to a

force tolerance of 0.01 eV/Å. The slab is of sufficient thickness such that the central layers exhibit bulk geometry without imposing constraints. Converged $2 \times 2 \times 1$ [$5 \times 5 \times 1$] MP k -point grids are employed for (2×2) [1×1] surface cells of both hematite and alumina. For computational speed, the r_{cut} was reduced to 3.5 Å, which has been shown to introduce less than 0.1 meV/Å² uncertainty into the surface energies, and a negligible effect on the forces.⁶⁹

A. Pb Benchmarking and Reference Structures. The experimental data used for benchmarking the computational studies of oxidized Pb compounds include the gas phase spectroscopy of the PbO molecular dimer,⁸⁰ and X-ray diffraction structures of crystalline α -PbO⁸¹ and β -PbO₂.⁸² In addition there are computational benchmarks for the rocksalt PbO crystal structure, and the Pb(OH)₂ molecular species. We implement the later as a simple, electrostatically neutral computational reference compound that should reflect the type of bonding exhibited by Pb adsorbed to hydroxylated surfaces. These benchmark compounds offer the important opportunity to compare the quality of our electronic structure methods in chemically distinct Pb environments, specifically spanning the Pb⁺² oxidation state ($5d^{10} 6s^2$) in Pb(OH)₂, PbO, and α -PbO, and the Pb⁺⁴ state ($5d^{10} 6s^0$) in β -PbO₂.

Calculations on the Pb benchmark species using the same level of theory employed for the hematite and alumina slabs (PBE XC, all-electron cores, double-numeric-polarization basis set, and $r_{cut} = 3.5$ Å) show excellent agreement with experimental values. For the PbO molecule, the errors are only 2.6% and 1.6% for r_{Pb-O} (1.922 Å) and for the vibrational frequency ω (720.96 cm⁻¹), respectively. For comparison, we indicate in Figure 2 the results obtained for both GGA-PBE and the Vosko–Wilk–Nusair local density approximation (LDA-VWN)⁸³ using (i) all-electron (AE) calculations, (ii) all-electron calculations with scalar relativistic corrections to the valence orbitals (referred to as VPSR),⁸⁴ and (iii) calculations using density functional semicore pseudopotentials (DSPPs)⁸⁵ for two bracketing values of r_{cut} . These values also compare favorably with the hybrid Hartree–Fock/DFT functional of Becke, three-parameter, Lee–Yang–Parr (B3LYP) and highly accurate coupled-cluster with single and double and perturbative triple excitations (CCSD(T)) results obtained by Benjelloun et al.⁸⁶ For the molecular species Pb(OH)₂, experimental data is not

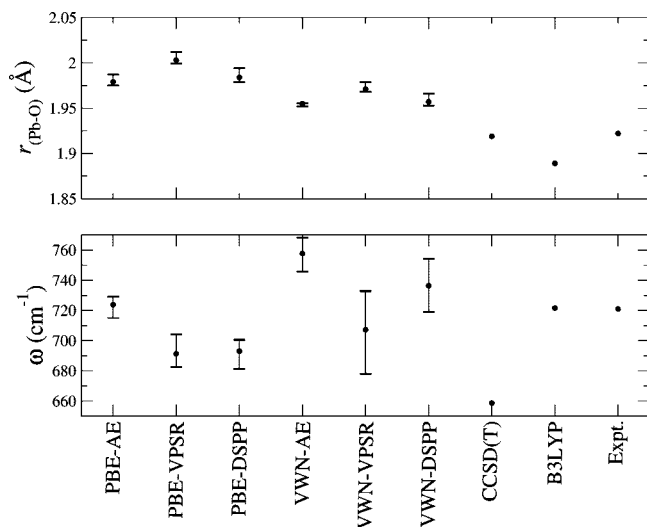


Figure 2. PbO dimer bond length, $r_{\text{Pb-O}}$ (Å) and vibrational frequency, ω (cm^{-1}) using PBE and VWN XC's in AE, VPSR, and DSPP calculations in DMol³. Error bars reflect variation in quantities as a function of $r_{\text{cut}} = 3.5\text{--}6.0$ Å. Also shown are values using CCSD (T) and B3LYP, taken from ref 86, and gas phase values from ref 80.

TABLE 1: Calculated bulk properties of α -PbO, rocksalt PbO, and β -PbO₂ compared to other theoretical studies^a

	a , Å	c , Å
α -PbO		
present	3.98 (−0.5%)	5.01 (0.0%)
other	4.06 (+2.5%)	5.39 (+7.6%)
expt.	3.96	5.01
PbO Rocksalt		
present	5.32	
other	5.27	
β -PbO ₂		
present	5.04 (+1.4%)	3.47 (+2.7%)
other	5.08 (+2.2%)	3.45 (+2.1%)
expt.	4.97	3.38

^a Other theoretical results taken from refs 89 and 90, in which DFT calculations were carried out using a pseudopotential approximation and the PBE functional.⁷⁴ Errors from experimental data, where available, are shown in parentheses. Values for α -PbO and β -PbO₂ are from refs 81 and 82, respectively.

available, but CCSD(T) benchmark calculations have been performed as it is hypothesized to be an important atmospheric species formed from Pb emissions.^{87,88} Our results of 2.136 Å for the Pb–O bond distance and 90.3° for the O–Pb–O angle are in close agreement with the CCSD(T) results, with deviations of 1.6% and 1.4%, respectively.

We carried out further testing of Pb–O bonding using consistent computational methods on bulk α -PbO and β -PbO₂ oxides. The magnitude of the c lattice constant in α -PbO reflects the accuracy of the description of the Pb 6s lone pair.⁸⁹ We achieve total energy convergence within 0.0051 eV with respect to k -point sampling using $4 \times 4 \times 4$ and $6 \times 6 \times 6$ MP k -point grids for α -PbO and β -PbO₂, respectively. As an additional test, we also consider PbO in a rocksalt crystal structure, on a converged $7 \times 7 \times 7$ MP grid.

Comparison of our theoretical bulk Pb oxide lattice constants with other theoretical and experimental (where available) results are presented in Table 1. We obtain theoretical lattice parameters for both oxides at a similar level of agreement with experiment. Our results for the in-plane Pb oxide lattice constants are consistent with other DFT studies using plane wave pseudo-

potential methods and the same XC.^{89,90} Using $r_{\text{cut}} = 3.5$ Å, our theoretical value of c achieves noticeably better agreement with experiment (Table 1). We investigated the effect of increasing r_{cut} to 4.5 Å, and found that in doing so, the error in c for α -PbO increased to 4.0%, while that of a for α -PbO and changes in the β -PbO₂ lattice constants were unremarkable. This shows a fortuitous ability to accurately model the Pb 6s lone pair while maintaining an efficient r_{cut} . Collectively, these results support the ability of our employed electronic structure methods to perform consistently and accurately across a range of possible Pb oxidation states and coordination environments.

B. Initial Pb Binding Geometries. Periodic (1×1) cells of (0001) (HO)₃–M–M–R surfaces are too small to model Pb(II) sorption on alumina within the reported realistic concentration ranges of (0.5 to 5.2) $\mu\text{mol}/\text{m}^2$,³⁰ and result in concentrations high in the reported range of (2.0 to 9.92) $\mu\text{mol}/\text{m}^2$ on hematite.²⁸ These higher concentrations on a (1×1) surface result in complicated adsorbate–adsorbate interactions, and/or polynuclear Pb(II)–surface complex formation, both of which are beyond the scope of the current study. In order to model Pb(II) sorption in a realistic coverage regime, we replicate the (1×1) surface cells into (2×2) supercells, on which one Pb atom/surface leads to coverages of (2.06 and 1.89) $\mu\text{mol}/\text{m}^2$ on alumina and hematite, respectively.

The structures of the fully hydroxylated O-terminated surfaces of α -Al₂O₃ and α -Fe₂O₃ contain several reasonable sites for initial Pb(II) binding geometries. Plausible Pb(II) coordination chemistry and the need to maintain a neutral nonpolar surface while constraining all surface species in their assumed environmental oxidation states are used to determine potential adsorption sites. The adsorbed structures are always charge balanced such that Pb is in the naturally dominant +2 oxidation state and hence Pb(II) is denoted by “Pb” from here on in.

The active sites at oxide surfaces are unsaturated anions, so the binding sites are defined by the surface oxygens. X-ray experiments have established the preferred trigonal pyramidal coordination of adsorbed Pb cations.³⁰ On the fully hydroxylated O-terminated surfaces, the oxygen layers are in a hexagonal lattice and the surface oxygen functional groups have trigonal symmetry. The topmost in-plane O–O distances are 2.61 Å to 2.96 Å on α -Al₂O₃, and 2.69 Å to 3.03 Å on α -Fe₂O₃. The centers of these oxygen triangles inherently provide a reasonable coordination environment for Pb. Note that we do not consider monodentate Pb adsorption (such as would be achieved by adsorbing Pb at oxygen top sites) because such binding modes have been ruled out by XAS studies.^{28,30}

A first-order evaluation of the fully hydroxylated O-terminated surfaces under study suggests similar reactivity at all sites, because each oxygen is coordinated to two cations in the surface. This is an oversimplification, as the (0001) corundum surface consists of a network of oxygen triangles that are structurally and chemically inequivalent due to the metal ion stacking in the octahedral sites below. Some oxygen triangles are centered about a metal cation just below the surface, whereas others are centered by an oxygen or cation deeper in the surface. These differences could be significant and thus investigating these sites separately is required.

We generate initial starting geometries for adsorbed Pb at surface sites centered about 3 surface hydroxyl groups, with Pb about 1.5 Å above the topmost surface O-plane, (corresponding to Pb–O bond lengths of about 2.1 Å based upon experimentally observed distances).^{28,30} We rely on alphanumeric labeling as shown in Figures 1 and 3 to name the adsorption sites in terms of the initial high symmetry locations: The M2

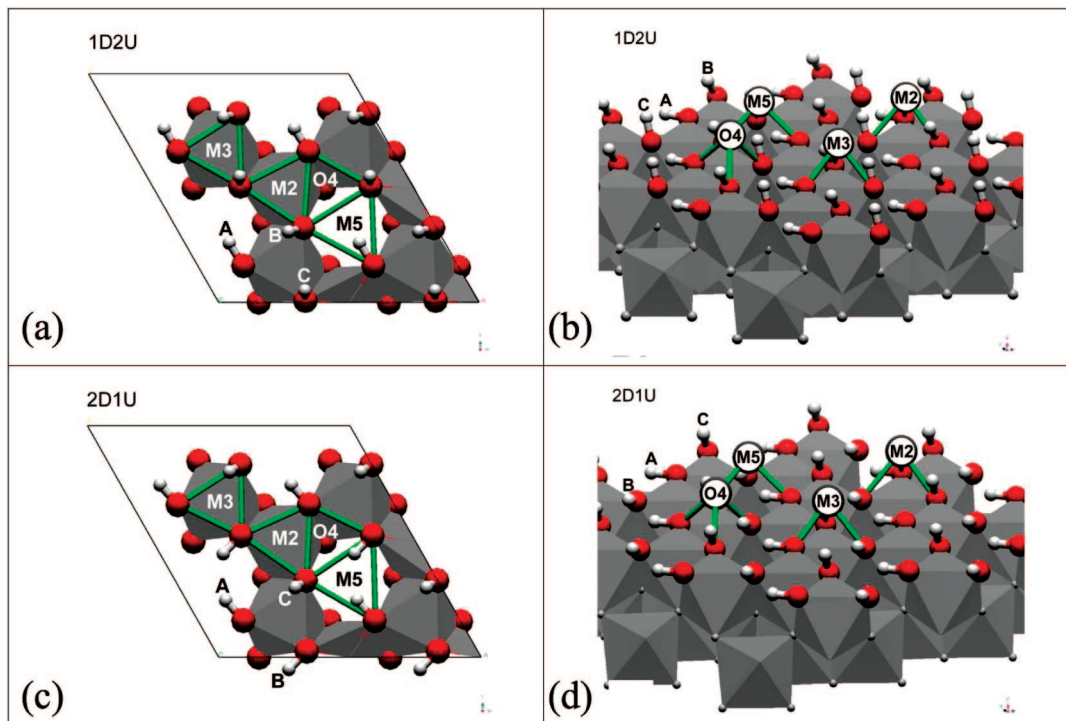


Figure 3. Fully hydroxylated oxygen terminated (0001) α - M_2O_3 surfaces. The initial Pb adsorption sites, M2, M3, O4, and M5 are indicated. H and O atoms are shown in white and red, respectively. MO_6 octahedra are indicated by gray polygons, which are centered by M cations. (a) Top view of the surface with the (1D2U) H-bond arrangement. The boundary of the (2×2) supercell is traced in black. Oxygen functional groups involved at each adsorption site are connected by green lines. The A, B, and C H^+ are labeled. (b) Perspective view of the surface with the 1D2U H-bond arrangement. Initial Pb positions for each site are indicated, with bonds to surface oxygens shown in green. The A, B, and C H^+ are indicated. (c) Same as (a), for the 2D1U H-bond arrangement. (d) Same as (b), for the 2D1U H-bond arrangement.

site is defined by a triangle of layer 1 O atoms centered above a M2 cation, the metal ion closest to the topmost oxygen layer. M3 is the site above the lower cation in the metal double layer. The O4 site is centered above a nonterminal oxygen layer atom. The M5 site, which is above the metal cation in the fifth atomic layer, corresponds to the bulk continuation site on the surface. The sites are shown schematically in Figure 3.

The M2, M3, O4, and M5 sites vary in how they relate to surface oxygen layers and the metal bilayers, in how the Pb interacts with surface MO_6 octahedra, and with respect to the arrangement of protons from surface hydroxyl groups. At the M2 and M3 sites, Pb is initially in a face-sharing configuration, interacting mainly with a single MO_6 octahedron. At the M5 and O4 sites, Pb is interacting with O atoms from multiple MO_6 octahedra. To maintain a charge neutral surface, 2 H^+ need to be displaced when Pb is introduced to an adsorption site. Details of the surface H-bonding and different H^+ displacement patterns are addressed below. In addition, we model Pb adsorption on both the top and bottom surfaces, to maintain the inversion symmetry of the slabs.

C. Electronic Structure Analysis Methods. Applying electronic structure methods to environmental molecular science is an exciting and new area of research. Several previous XAS studies employ the intuitive bond-valence model,⁹¹ with a more accurate description of O–H bonding.³⁶ Each bond formed by an atom has a bond valence value which can be interpreted as the fraction of valence (or charge) distributed between neighboring atoms in a bond. This empirical tool can be used to predict bonding arrangements that satisfy the assumption of local charge balance based on formal valence states of atoms. Using DFT in the present study, we are able to probe details of Pb(II) bonding interactions at a molecular level.

A main goal of this comparative study is to relate surface composition to reactivity. We define the Pb adsorption energy, E_{ads}

$$E_{\text{ads}} = \frac{1}{2}[(E_{\text{surf}} + 2E_{\text{Pb(OH)}_2}) - (E_{\text{surf/Pb}} + 4E_{\text{H}_2\text{O}})] \quad (1)$$

where E_{surf} and $E_{\text{surf/Pb}}$ are the total energies of the hydrated surface and the hydrated surface with two H^+ displaced by Pb, respectively, $E_{\text{H}_2\text{O}}$ is the total energy of an isolated water molecule, and $E_{\text{Pb(OH)}_2}$ is the total energy of the isolated gas-phase Pb complex. Division by 2 accounts for the two equivalent surfaces. Under this sign convention, positive values represent favorable adsorption.

To identify and characterize bonding mechanisms, we analyze the electronic structure using both deformation density and projected density of states. To visualize the bonding in adsorbed Pb, we study the deformation density ρ_d defined within DMol³ as

$$\rho_d = \rho_r - \sum_{\alpha} \rho_{\alpha}(r - R_{\alpha}) \quad (2)$$

where ρ_r is the system charge density and $\rho_{\alpha}(r - R_{\alpha})$ is the density of the free atom α located at coordinates R_{α} . Regions of $\rho_d > 0$ indicate bond formation, whereas $\rho_d < 0$ indicate electron loss relative to the gas phase neutral atomic species.

Another useful means of analyzing surface electronic structure is in terms of the density of states (DOS), a measure of the distribution of electronic energy levels in the system. The DOS can be used comparatively for different surfaces to determine the relative number of states available for adsorbate interactions above and below the surface's highest occupied energy level (or Fermi energy, E_F). In order to represent the surface electronic

TABLE 2: Calculated layer spacings d (Å) and percent relaxations Δ with respect to bulk Al_2O_3^a

layers	surface		Al2		Al3		Al5	
	1D2U		$E_{\text{ads}} = -0.18$ eV		$E_{\text{ads}} = 0.23$ eV		$E_{\text{ads}} = 0.07$ eV	
	d	Δ	d	Δ	d	Δ	d	Δ
O1–Al2	0.908	8.4	0.925	10.4	0.899	7.3	0.905	7.9
Al2–Al3	0.317	–37.6	0.300	–41.0	0.361	–28.9	0.329	–35.2
Al3–O4	0.933	11.3	0.953	13.8	0.918	9.5	0.935	11.5
O4–Al5	0.817	–2.6	0.843	0.6	0.843	0.6	0.839	0.1

layers	surface		Al2		Al3		Al5	
	2D1U		$E_{\text{ads}} = -0.02$ eV		$E_{\text{ads}} = 0.28$ eV		$E_{\text{ads}} = 0.36$ eV	
	d	Δ	d	Δ	d	Δ	d	Δ
O1–Al2	0.900	7.4	0.920	10.4	0.892	6.5	0.910	8.6
Al2–Al3	0.336	–33.8	0.306	–39.7	0.371	–26.9	0.336	–33.8
Al3–O4	0.932	11.3	0.952	13.6	0.915	9.2	0.932	11.2
O4–Al5	0.846	0.9	0.845	0.9	0.846	0.9	0.844	0.7

^aTheoretical bulk layer spacings are 0.838 Å between Al–O layers and 0.508 Å between Al–Al layers. Values of E_{ads} are calculated according to eq 1 and reported in eV. Detailed descriptions of the Pb/Al₂O₃ geometries and naming schemes are given in the text.

structure in a chemically intuitive manner, partial density of states (PDOS) analysis is employed. This semiquantitative method deconstructs the charge density into components from each atom, and for each atom, determines the s, p, and d character of the DOS. Hybridization leading to covalent interactions can be identified and traced to specific states of specific atoms through PDOS analysis.⁹² In the spin-polarized hematite surfaces, the DFT eigenvalues differ between the two spin states, resulting in two PDOS data sets for each atom. As the DFT spin axis is arbitrary, the PDOS for opposite sign spins are labeled as majority and minority based on relative occupations.

III. Results and Discussion

Our discussion of results begins with the hydrated oxide surfaces, providing a basis for understanding reactivity in terms of surface geometry and electronic structure. We report values of E_{ads} on α -Al₂O₃, spanning an extensive range of adsorption sites, H⁺ deprotonation patterns, and H-bonding networks. We determine an appropriate commensurate subset of Pb adsorption geometries to model on the hematite surface, and summarize the resulting trends in E_{ads} . The remainder of the discussion highlights aspects of geometry and electronic structure of Pb/M₂O₃ (0001) extracted from our DFT calculations, and application of these results to providing an improved molecular level understanding of Pb sorption.

A. Surface H-Bond Networks. The impact of surface hydroxyl group orientation on hydrated surface reactivity has not been investigated prior to this work. X-ray methods are insensitive to protons, which makes possible hydrogen geometries a key consideration for modeling studies. Static first-principles studies on the hydrated α -Al₂O₃ (0001) surface have focused on finding the overall minimum energy surface structure. Room temperature dynamic simulations^{49,50} have shown that on average, 1 out of every 3 surface OH groups lies in the surface plane on α -Al₂O₃ (0001), participating in intralayer H-bonding. These in-plane OH groups span the Al5 (bulk cation) sites, whereas the other 2 out of 3 OH groups are nearly perpendicular to the surface. At 300 K, OH patterns were found to lock in on a scale of about 0.1 ps and to evolve over longer periods. Static DFT calculations support that structures with 1 out of 3 OH groups participating in intralayer H-bonding is the minimum energy structure.^{93,94} Sum-frequency vibrational spectroscopy has also been used to study surface dipole orientations and surface charging in water.³⁹

We hypothesize that the complex and dynamic H-bond structure observed on α -Al₂O₃ (0001) may sterically influence reactivity through blocking of adsorption sites. To more realistically model adsorption through static calculations, it is therefore necessary to explore different OH orientations that may be energetically accessible under realistic conditions. We model six unique hydrogen bond arrangements in (1 × 1) surface cells of both alumina and hematite. Under periodic conditions, these H-bond patterns form ordered surface H-bond networks. From several starting structures, we arrive at two minima. We find that the lowest energy H-bond network for both the Al₂O₃ and Fe₂O₃ surfaces is the previously reported structure for Al₂O₃, with 1 out of 3 OH groups spanning the M5 site, as shown in Figure 3. We refer to this surface H-bonded structure as “1D2U”, for “one (H⁺) down, two (H⁺) up”. A second H-bond network (not previously reported), which is essentially equivalent in energy (0.04 and 0.03 eV higher in energy for alumina and hematite, respectively) was also observed. We refer to this second arrangement as “2D1U”, for “two (H⁺) down, one (H⁺) up”. Top views of the two hydrogen bond arrangements are shown in Figure 3, where we also label the various protons as A, B, and C H⁺. On the α -Al₂O₃ (0001) 1D2U surface, the hydroxyl groups are directed out of the surface plane by 0.18°, 55.80°, and 69.2° for A, B, and C, respectively. On the 2D1U surface, the values are 3.37°, 23.40°, and 65.03° for A, B, and C, respectively.

While the 1D2U and 2D1U structures are energetically similar, the 2D1U structure is qualitatively unique in that 2 out of every 3 OH groups span the M5 site. In the global minimum 1D2U, one OH group forms two hydrogen bonds to surface O atoms, whereas in the 2D1U structure, two OH groups form hydrogen bonds to the same surface O atom. We tabulate the layer spacings (and the deviations from bulk positions), in Tables 2 and 3 for Al₂O₃ and Fe₂O₃, respectively. To our knowledge, 2D1U is a novel structure that has not yet been identified for any adsorption processes on alumina or hematite.

Our identification and study of a second H-bond network allows us to systematically compare the influence of hydrogen steric effects on different adsorption sites. On α -Al₂O₃ (0001), we model Pb adsorption in the presence of both surface H-bond networks. With four possible adsorption sites, two H-bonded surface networks, and three unique deprotonations per adsorption site leads to a total of 24 starting structures for Pb adsorption. On the 1D2U surface, we label the 3 initial structures for each

TABLE 3: Calculated layer spacings d (Å) and percent relaxations Δ with respect to bulk Al_2O_3 ^a

layers	surface		Fe2		Fe3		Fe5	
	1D2U		$E_{\text{ads}} = -1.21$ eV		$E_{\text{ads}} = 0.86$ eV		$E_{\text{ads}} = 0.76$ eV	
	d	Δ	d	Δ	d	Δ	d	Δ
O1–Fe2	0.924	11.0	1.007	20.9	0.931	11.7	0.932	11.8
Fe2–Fe3	0.518	–20.4	0.379	–41.7	0.549	–15.3	0.504	–22.5
Fe3–O4	0.898	7.8	0.952	14.3	0.878	5.4	0.902	8.5
O4–Fe5	0.830	–0.4	0.828	–0.6	0.837	0.5	0.831	–0.3

layers	surface		Fe2		Fe3		Fe5	
	2D1U		$E_{\text{ads}} = 1.56$ eV		$E_{\text{ads}} = 0.89$ eV		$E_{\text{ads}} = 1.03$ eV	
	d	Δ	d	Δ	d	Δ	d	Δ
O1–Fe2	0.872	4.7	0.970	16.5	0.896	7.6	0.927	11.3
Fe2–Fe3	0.545	–16.1	0.416	–36.0	0.573	–11.9	0.511	–21.3
Fe3–O4	0.890	6.9	0.938	12.6	0.870	4.4	0.900	8.1
O4–Fe5	0.825	–1.0	0.841	0.9	0.839	0.7	0.833	0.0

^aTheoretical bulk layer spacings are 0.833 Å between Fe–O layers and 0.650 Å between Fe–Fe layers. Values of E_{ads} are calculated according to Equation 1 and reported in eV. Detailed descriptions of the Pb/ Al_2O_3 geometries and naming schemes are given in the text.

TABLE 4: Values of E_{ads} (eV) for Pb/ α - M_2O_3 (0001)^a

	1D2U			2D1U		
	A	B	C	A	B	C
			Al_2O_3			
Al2	–0.18	–0.38	–0.77	–0.02	–0.55	–0.19
Al3	0.23	–0.02	–0.25	0.28	0.23	0.02
O4	0.07	–0.01	–0.77	–0.47	–0.99	0.10
Al5	0.07	0.12	0.12	0.06	0.13	0.36
			Fe_2O_3			
Fe2	1.21			1.56		
Fe3	0.86			0.89		
Fe5			0.76			1.03

^aThe adsorption site naming scheme is described in the text.

site A, B, and C indicating which of the three H^+ protons (first in-plane, second in-plane, and out-of-plane respectively) are left intact. On the 2D1U surface, the deprotonation patterns are labeled A, B, and C corresponding to when the first in-plane, second in-plane, or the out-of-plane hydroxyl group are left protonated, respectively.

B. Trends in Adsorption Energy I: Pb/ α - Al_2O_3 (0001).

The results for our calculated E_{ads} for each of the 24 modeled Pb/ Al_2O_3 structures is presented in Table 4. Notably, both the preferred site and choice of H^+ displacement differs between the 1D2U and 2D1U H-bonded surfaces: On the 1D2U surface we observe that the Al3A site is most favorable ($E_{\text{ads}} = 0.23$ eV). The 2D1U Al3A site is slightly more favorable than on the 1D2U surface, with $E_{\text{ads}} = 0.28$ eV, however the 2D1U Al5C site is overall the most favored site, with $E_{\text{ads}} = 0.36$ eV.

On the 1D2U surface, the most favorable H^+ displacement for almost all sites is A, which leaves the in-plane hydroxyl group at the site intact. The single exception is at Al5, where C H^+ displacement, which deprotonates the in-plane hydroxyl group, is preferred. The outlying preference for C over A deprotonation at 1D2U Al5 can be understood by recalling that the in-plane OH groups span the Al5 site (Figure 3). The 1D2U Al5A site is sterically blocked in the fully hydroxylated surface. C H^+ displacement opens this site for Pb adsorption. At all of the other 1D2U sites (Al2, Al3, and O4), the in-plane hydroxyl group is directed away from the site, and it is preferable to maintain the stabilizing intralayer surface H-bonding by displacement of the A H^+ .

The most favorable Pb adsorption is at Al5C on the 2D1U surface, with $E_{\text{ads}} = 0.36$ eV (Table 4). This agrees with the

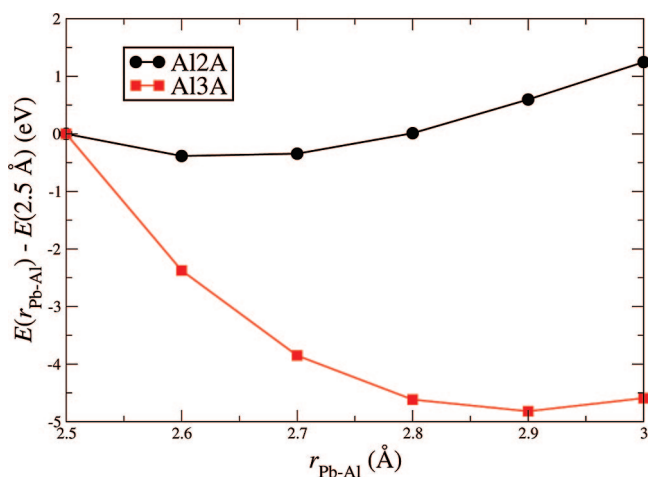


Figure 4. Total energies as a function of Pb–Al separation ($r_{\text{Pb-Al}}$, Å) for the Al2A and Al3A geometries on the 1D2U H-bonded surface. Each curve is referenced to the total energy at $r_{\text{Pb-Al}} = 2.5$ Å.

intuition that the bulk cation site is preferred. Pb adsorption at this site minimizes cation–cation interaction associated with the face-sharing Al2 and Al3 sites. The fact that E_{ads} at Al5C on the 2D1U surface is favored by 0.24 eV relative to the 1D2U surface can be explained by examining the Pb absorption-induced OH relaxations. On the 2D1U surface, greater relaxation of the intact hydroxyl group into the surface plane (and away from Pb) results in stabilization contributing to a more favorable E_{ads} . The impact of this hydroxyl group relaxation is not obvious in the tabulated layer spacings reported in Table 2 but can be seen in Figure 1.

When the Al5 site is blocked by intraplanar H-bonding, the most favorable site is Al3A. We can interpret that the preference of the A H^+ displacement pattern at the Al3 site is due to the stabilizing intraplanar H-bonding. To understand why the Al3 site is preferred over the Al2 site, we consider how the Pb–Al separation, $r_{\text{Pb-Al}}$, affects the total energy at each cation site. We calculate interaction curves by taking the Al2A and Al3A initial configurations on the 1D2U surface (with Pb centered above subsurface Al2 and Al3 atoms, respectively) and varying $r_{\text{Pb-Al}}$ from 2.5 Å to 3.0 Å. No geometry optimization is carried out. The results are plotted in Figure 4. The plot shows that while the interaction curve for Al3A is attractive, the Al2A curve is actually repulsive for $r_{\text{Pb-Al}} > 2.7$ Å. This reflects the balance of $r_{\text{Pb-O}}$ with $r_{\text{Pb-Al}}$: In the optimized Al2 structure, the average

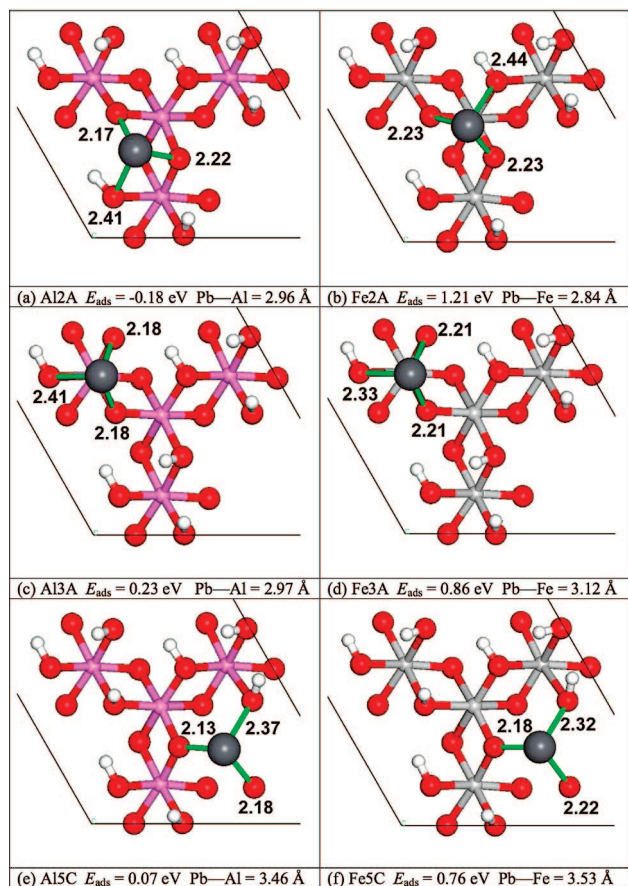


Figure 5. Top views of the optimized Pb/M₂O₃ geometries on the 1D2U H-bonded surfaces. Al, Fe, O, H, and Pb are shown in magenta, light gray, red, white, and dark gray, respectively. Pb–O bonds are drawn in green, and $r_{\text{Pb–O}}$ distances are labeled (in Å). Structure names, values of E_{ads} , and the shortest Pb–M separations are indicated in each panel.

value of $r_{\text{Pb–O}}$ ranges from 2.27 to 2.65 Å for $r_{\text{Pb–Al}} = 2.5$ Å to 3.0 Å, while in the optimized Al3A structure, $r_{\text{Pb–O}}$ ranges from 1.98 to 2.34 Å for $r_{\text{Pb–Al}} = 2.5$ Å to 3.0 Å. From our above benchmarking of Pb–O distances, and from XAS experiments that report $r_{\text{Pb–O}}$ in the range of 2.18 Å to 2.35 Å in Pb/Al₂O₃ samples, we conclude that the Al3A site offers an inherently more favorable balance between Pb–Al repulsion and Pb–O attraction.

Although H-bonding strongly influences α -Al₂O₃ (0001) surface stability, Pb adsorption does not show a simple preference to maximize the extent of intraplanar H-bonding. Stabilizing H-bonding can also lead to deactivation of deprotonated surface oxygens. This can be illustrated by comparing the most preferred adsorption site on the 1D2U surface (Al3A, $E_{\text{ads}} = 0.23$ eV) and the most preferred adsorption site on the 2D1U surface (Al5C, $E_{\text{ads}} = 0.36$ eV). In the 1D2U Al3A structure, there is more extensive intraplanar H-bonding in the (2 × 2) surface than in the 2D1U Al5C structure. As can be seen in Figure 5, the 1D2U Al3A structure has reactive oxygens participating in both Pb adsorption and as acceptor sites for intraplanar H-bonds. From a bond valence perspective, the H-bonding results in greater saturation of the oxygen sites, decreasing their capacity to bond with Pb and therefore resulting in weaker E_{ads} .

Only through consideration of a second, nearly energetically degenerate surface H-bond network do we arrive at the global minimum energy Pb/Al₂O₃ structure. The differing Pb site

preference on 1D2U and 2D1U results from a balance of stabilizing intraplanar H-bonding, steric site blocking, and surface functional group reactivity. These results demonstrate the need to consider details beyond the coordination of surface functional groups in predicting reactivity trends on hydrated oxide surfaces.

C. Trends in Adsorption Energy II: Pb/ α -Fe₂O₃ (0001).

From the 24 optimized Pb(II)/Al₂O₃ structures, we highlight a subset of the adsorption sites to consider in the Pb/Fe₂O₃ system. Based on the role of intraplanar H-bonding and steric effects observed on alumina, we select Fe2A, Fe3A, and Fe5C on both the 1D2U and 2D1U surfaces for further discussion. The resulting values of E_{ads} are presented in Table 4.

In agreement with experiment, our DFT results show stronger Pb binding on α -Fe₂O₃ (0001) than on α -Al₂O₃ (0001).⁸ We observe this order of reactivity through consideration of only the isostructural (fully hydroxylated, oxygen terminated) surface. The difference in adsorption strength is notable, as E_{ads} on alumina is only about 23% of that on hematite. This is new evidence that composition and not solely structure dictates important reactivity trends on hydrated oxides. Additionally, we report that the Fe2 site, not the bulk cation site, to be most preferred by Pb. The Pb site preference is unaffected by the surface H-bond network. The differing site preference and adsorption strength on the isostructural surfaces indicates fundamentally different electronic interactions between Pb and the surfaces of the two oxide compositions.

D. Comparison of Pb Binding Geometries on α -Al₂O₃ (0001) and α -Fe₂O₃ (0001).

The initial Pb binding geometries are described in section II.C and shown in Figure 3. The initial sites are highly symmetric with respect to the oxygen sublattice. Upon optimization, Pb shifts off-center, elongating the Pb–OH separation while maintaining shorter distances to the surface oxo-functional groups. The result is highly asymmetric structures with respect to the triangular oxygen sublattice. Details of the optimized Pb/M₂O₃ geometries are presented in Figures 5 and 6 for the 1D2U and 2D1U surfaces, respectively.

The structural details of our DFT Pb/M₂O₃ structures show overall good agreement with experimental information. For Pb/Al₂O₃, our DFT Pb–O are at most 0.07 Å below, and 0.13 Å above, the reported XAS ranges for Pb bonds with oxo and hydroxo groups, respectively.³⁰ For Pb/Fe₂O₃, our DFT Pb–oxo(hydroxo) bond lengths are at most 0.118 (0.191) Å shorter (longer) than the average XAS Pb–O distance of 2.28 Å in powder iron oxide samples. Our Pb–Al distances, as shown in Figures 5 and 6, are in reasonable agreement with XAS ranges of 3.16 Å–3.32 Å in powder aluminum oxide samples.³⁰ Our results for Pb–Fe distances do include some values <3.0 Å, outside of the 3.27 Å to 3.26 Å range derived from XAS studies on powder iron oxide samples.²⁸ Due to the lack of experimental data specifically for Pb/Fe₂O₃ (0001), and based on the good agreement between the XAS range and many of our DFT Pb–Fe distances, our structural results are reasonable.

E. Electronic Structure of Pb/Al₂O₃ and Pb/Fe₂O₃: PDOS.

Electronic structure calculations provide a powerful means to assess the differences in surface chemistry between alumina and hematite. PDOS analysis of atoms in the outermost layers allows us to contrast the bonding between the surface cations and oxygen in the two oxides.⁹⁷ The PDOS for the hydrated α -Al₂O₃ (0001) surface is shown in Figure 7. We project the DOS locally onto atoms from the topmost O layer (O1) and 2 topmost cation layers (Al2 and Al3, as shown in Figure 1). The s and p contributions are shown for both O and Al atoms. A wide energy range (20 eV below to 25 eV above E_{F} , which is set to zero) is

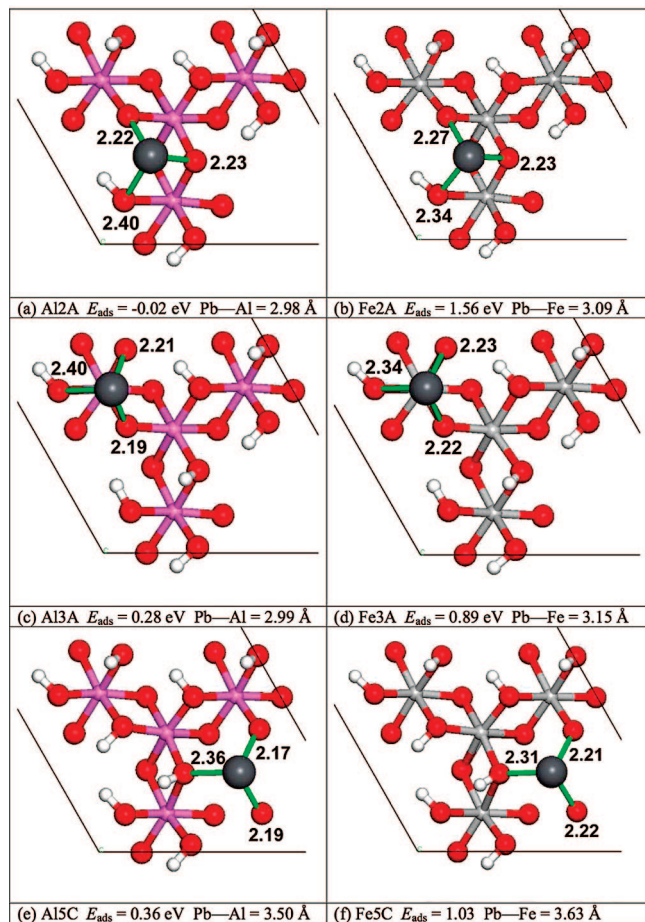


Figure 6. Same as Figure 5, for the 2D1U H-bonded surfaces.

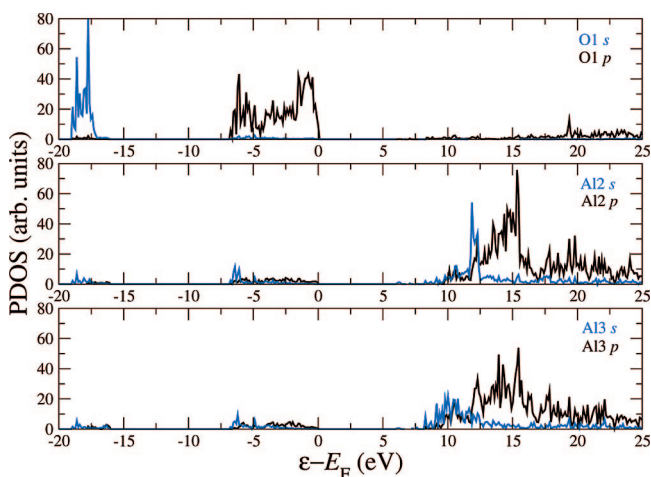


Figure 7. PDOS of the hydrated Al_2O_3 surface. E_F is set to $x = 0$. Top: Layer 1 O s (blue) and p (black) PDOS. Middle: Al2 cation s (blue) and p (black) PDOS. Bottom: same as middle panel, for the Al3 cation.

used to show both low-lying core states and high-lying empty states. While there is some mixing between O and Al states from about -7 eV to E_F , the PDOS shows that the surface Al–O interaction is mainly ionic: Most of the O1 s and p PDOS intensity is below E_F , and most of the Al2 (and Al3) s and p PDOS intensity is above E_F .

The PDOS for the hydrated $\alpha\text{-Fe}_2\text{O}_3$ (0001) surface atoms is shown in Figure 8. Again, we focus on the topmost oxygen layer (O1), and the two cation layers of the topmost Fe bilayer (Fe2 and Fe3, see Figure 1). The surface chemistry of hematite

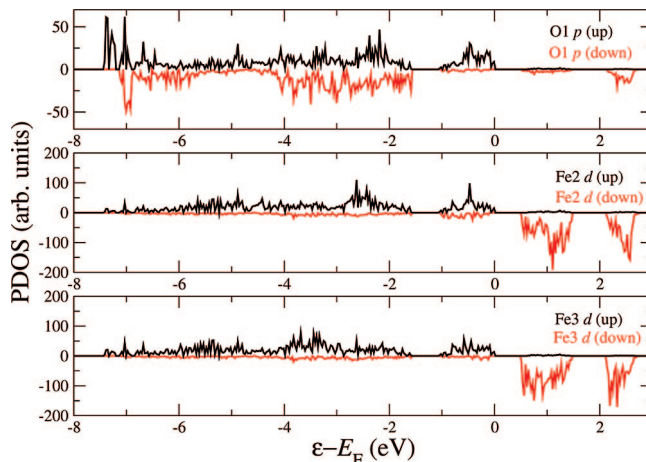


Figure 8. PDOS of the hydrated Fe_2O_3 surface. E_F is set to $x = 0$. Top: Layer 1 oxo p majority (positive, black) and minority (negative, red) PDOS. Middle: The Fe2 cation 3 d majority (positive, black) and minority (negative, red) PDOS. Bottom: same as top panel for the Fe3 cation.

is influenced by covalent Fe 3 d–O 2 p interactions. We do not show the O 2 s PDOS, which shows the same core state behavior as can be seen in alumina in Figure 7. The covalency of the surface also leads to empty states closer to E_F , and we use a more narrow energy range to highlight the hematite surface chemistry than on the strongly ionic, structurally analogous alumina surface. The nearly octahedral Fe coordination causes the 3d states to split into approximate e_g bonding and t_{2g} antibonding states. The different occupations of the majority and minority Fe 3 d bands are clear by the PDOS intensity below and above E_F . Figure 8 also shows strong similarity between the Fe2 and Fe3 d–PDOS.

Individually, the PDOS show the bonding interactions present in each of the surfaces. Comparatively, we note that in $\alpha\text{-Al}_2\text{O}_3$ (0001), the relatively wide gap leaves the surface deficient in empty states near E_{FF} . The DOS around E_{FF} has been shown to play an essential role in reactivity,⁹² as both charge transfer and orbital mixing require available states. Owing to the partially filled Fe d-band, the PDOS of $\alpha\text{-Fe}_2\text{O}_3$ (0001) exhibits relatively low-lying empty states. Additionally, the more covalent character in hematite leads to a more diffuse distribution of oxygen states.

The PDOS of Pb/ M_2O_3 is employed to determine the electronic origins of stronger E_{ads} on hematite, as well as to explain the composition dependence of Pb site preference. We plot the PDOS of the Al5C 2D1U structure, which shows the strongest Pb binding out of all of our modeled geometries on alumina, in Figure 9. The Pb is strongly ionized, as can be seen from the strong s and p PDOS intensity below and above E_F , respectively. Some Pb–O covalent mixing, particularly between Pb s, Pb p, and O p states, is present near the top of the valence band. Figure 9 also shows the PDOS of an Al2 atom (in the metal ion layer closest to the terminating oxygen layer), in the Al5C 2D1U geometry. This Al2 PDOS shows unremarkable variation with respect to the PDOS of the analogous atom in the hydrated surface without Pb, shown in Figure 7. Not shown, but also considered, were the PDOS of different Al2, Al3, and Al5 atoms in several Pb/ Al_2O_3 structures, including Al2 and Al3 sites. These investigations did not reveal any meaningful differences between the PDOS of Al cations in the Pb adsorbed structures versus Al in the hydroxylated surface. We conclude that the role of surface cations is limited to ionic-covalent

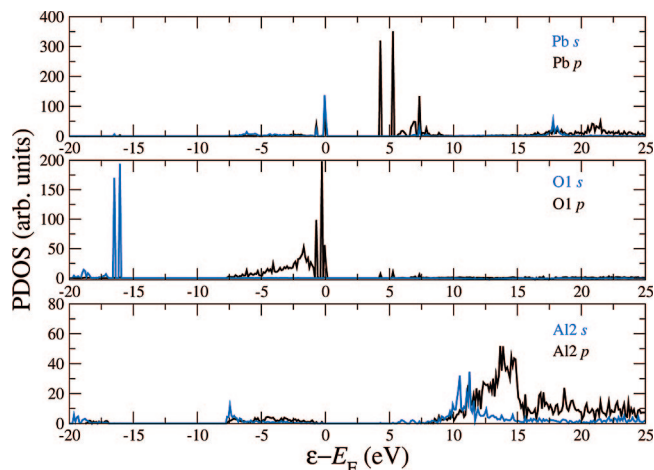


Figure 9. PDOS of Pb/Al₂O₃ in the Al5C 2D1U geometry. E_F is set to $x = 0$. Top: The Pb s (blue) and p (black) PDOS. Middle: Layer 1 oxo s (blue) and p (black) PDOS. Bottom: The Al2 s (blue) and p (black) PDOS.

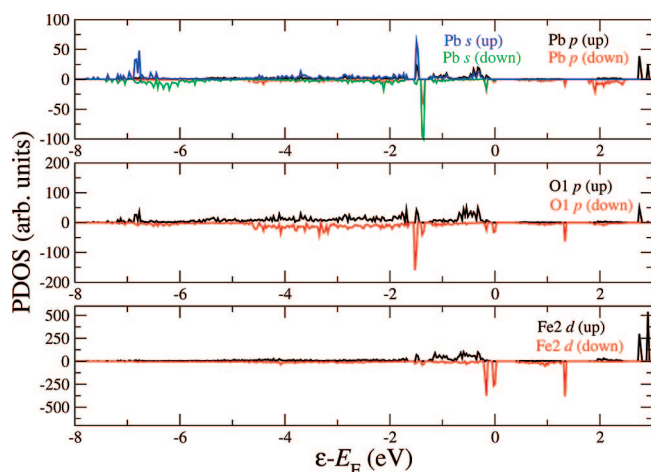


Figure 10. PDOS of Pb/Fe₂O₃ in the F2A 2D1U geometry. E_F is set to $x = 0$. Top: The Pb s majority (positive, blue) Pb s minority (negative, green), Pb p majority (positive, black), and Pb p minority (negative, red) PDOS. Middle: Layer 1 oxo p majority (positive, black) and minority (negative, red) PDOS. Bottom: The Fe2 3 d majority (positive, black) and minority (negative, red) PDOS.

interactions with oxygen, and they do not participate in the Pb/oxide binding in alumina.

We report the PDOS of Pb/Fe₂O₃ to address both the stronger Pb adsorption relative to alumina and the disparate trends in Pb site preference on hematite. E_{ads} is greater at each site on hematite relative to the analog sites on alumina (Table 4). The Pb site preference on hematite for the Fe2A (regardless of the H-bonding in the surface) is substantial, with E_{ads} being at least 42% greater than at the Fe3A site.

The PDOS of the Fe2A 2D1U structure (the global minimum, with $E_{\text{ads}} = 1.56$ eV) is shown in Figure 10. Again, Pb–O covalency is seen. Compared to the Pb–O covalent bonds in Pb/Al₂O₃, which are mainly located within 0.5 eV of E_F , the Pb–O covalent interaction is more stable in Pb/Fe₂O₃, showing intensity in the range of about 1 eV to 1.5 eV below E_F . Strikingly, the d-band of the Fe2 cation shows significant variation to its counterpart in the Pb-free hydroxylated surface. The electronic structure of Fe cations in the hydrated surface (Figure 8) show mainly filled(empty) spin majority(minority) d-bands. In the Pb Fe2A geometry, both the majority and minority d-bands are split such that each has filled (below E_F)

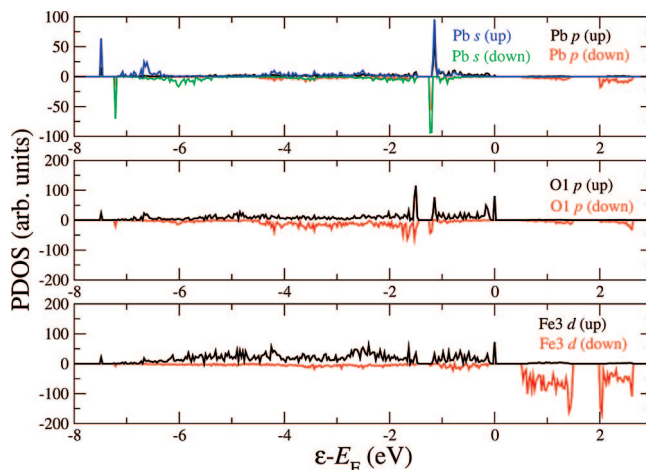


Figure 11. PDOS of Pb/Fe₂O₃ in the F3A 1D2U geometry. E_F is set to $x = 0$. Top: The Pb s majority (positive, blue) Pb s minority (negative, green), Pb p majority (positive, black), and Pb p minority (negative, red) PDOS. Middle: Layer 1 oxo p majority (positive, black) and minority (negative, red) PDOS. Bottom: The Fe3 3 d majority (positive, black) and minority (negative, red) PDOS.

and empty (above E_F) states. The new antibonding state in the spin majority Fe2 d-band overlaps with O1 p-PDOS and Pb p-PDOS. The new bonding states in the minority Fe2 d-band overlap with O1 p-PDOS and with both Pb s and p-PDOS. This break down of orbital mixing in Pb/Fe₂O₃ is consistent with theoretical work on the origin of asymmetric electron density in α -PbO.⁹⁵ The overlap of Pb, O, and Fe states shows that Fe can directly participate in Pb adsorption. A complimentary analysis of what is shown visually in Figure 10 can be made through Mulliken spin population analysis. In the hydroxylated α -Fe₂O₃ (0001) surface, the net spin on the topmost Fe cation in the bilayer is 3.66 μ_B . In the Fe2A Pb adsorbed structures, the net spin is reduced to about 0.9 μ_B . These analyses explain the fact that Fe2A (on both 1D2U and 2D1U surfaces) exhibits the strongest Pb binding. The stabilizing effect of lowering the net spin on the topmost Fe layer is the subject of a further study addressing the role of spin states in hematite surface stability and reactivity.

Not shown is the Fe2A 1D2U PDOS, in which similar Pb–O covalency and Pb–O–Fe mixing are observed. While most favored on the hematite 1D2U surface, this structure trails the Fe2A 2D1U global minimum, as measured through weaker (by 0.35 eV) E_{ads} . Structural comparison (Figures 5 and 6) shows that Pb off-centers more from the initial Fe2 site on the 2D1U surface than in the higher energy configuration found on the 1D2U surface. Therefore, while more subtle than on the alumina surface, H-bonding does influence the Pb binding geometry. We conclude that a more optimal balance of steric interactions, cation repulsion, and covalent mixing is achieved in Fe2A 2D1U.

In contrast to the Fe2 site, in Fe3A 2D2U there is little variation between the Fe d PDOS on the Pb adsorbed (Figure 11) and bare hydroxylated surface (Figure 8). This establishes that covalent Pb–O mixing contributes to E_{ads} on both alumina and hematite, but leads to greater stabilization in Pb/Fe₂O₃ owing to the partially filled Fe d-band. This indirect effect is nonlocal, and arises from the covalent nature of the hematite surface. The additional stability achieved through Pb–O–Fe mixing seen at the Fe2A site depends strongly on the geometry of Pb adsorption.

F. Electron Density of Pb/Al₂O₃: ρ_d . We visualize the shape of the charge density at the Pb adsorbed interfaces through ρ_d ,

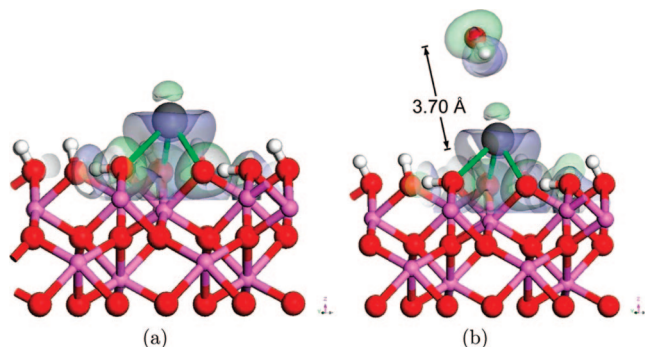


Figure 12. ρ_d of Pb/Al₂O₃ at the 1D2U Al3 site, in the absence (a) and presence (b) of an added H₂O molecule. Green isosurfaces show $\rho_d > 0$, while blue isosurfaces show $\rho_d < 0$. Pb–O bonds are indicated in green. Pb, O, H, and Al atoms are shown in dark gray, red, white, and light gray, respectively.

calculated according to Equation 2. This qualitative analysis⁹⁸ reveals the directionality of the Pb lone pair. As shown in Figure 12, the lone pair is directed away from the surface, in agreement with predictions from experimental investigations.²⁸ This shape consistently appears in all of our Pb/M₂O₃ structures.

The undeviating shape of ρ_d across our Pb/M₂O₃ structures enables us to study interactions between adsorbed Pb and additional species above the surface in a subset of geometries. In particular, we select the addition of a water of hydration to a Pb/Al₂O₃ structure (1D2U Al3) as a model for H₂O–Pb lone pair interaction. Initially, H₂O is placed 1.85 Å above adsorbed Pb in the surface normal direction. Upon DFT geometry optimization, the Pb–O_{H₂O} distance is 3.70 Å, as shown in Figure 12. The plotted ρ_d shows no charge transfer between H₂O and the adsorbed Pb complex. Additionally, we compute the adsorption energy of the water of hydration, $E_{\text{ads,H}_2\text{O}}$, to be <0.1 eV. Exploratory modeling of an additional H₂O to other Pb/M₂O₃ structures results in $E_{\text{ads,H}_2\text{O}}$ and Pb–O_{H₂O} distances of similar magnitude, and unremarkable differences in ρ_d . These results allow us to characterize the Pb lone pair as hydrophobic, supporting the validity of modeling Pb adsorption as an inner-sphere complex in the absence of additional waters of hydration.

IV. Conclusions

We have carried out a comparative study of Pb(II) binding on isostructural alumina and hematite hydrated surfaces using periodic DFT calculations. Pb adsorption is modeled on the fully hydroxylated, oxygen terminated surface stoichiometry, (HO)₃–M–M–R, believed to be the exclusive phase on alumina^{48,70} and the dominant on hematite.⁶⁹

Our DFT results reproduce the experimentally established trend in surface reactivity that Pb adsorption on α -Fe₂O₃ (0001) \gg α -Al₂O₃ (0001).⁸ Our optimized Pb/M₂O₃ geometries are also reported to be in reasonable agreement with XAS studies of powder systems.^{28,30} The analysis of the atomic and electronic structure of these systems leads to a new understanding of how interface structure and composition influence reactivity.

On the less reactive α -Al₂O₃ (0001) surface, we report a strong dependence of Pb(II) adsorption strength and geometry on the surface H-bonding. We only obtain an energetic preference for Pb binding at the bulk-like cation surface site on one of two studied H-bonded surfaces. We also report that maximizing intraplanar H-bonding is not a successful method for predicting the most stable Pb/Al₂O₃ geometries, as it can lead to bonding competition between in-plane H atoms and adsorbing Pb. The periodicity used in our calculations models

H-bond networks as uniform domains. We note that such domains are likely to dynamically exist, in different sizes, with different local H-bonding patterns. Consideration of surface hydroxyl group orientation should be explored in static modeling of similar H-bonded surfaces. On the more reactive α -Fe₂O₃ (0001) surface, we note far less influence of the surface H-bonding on the Pb(II) adsorption properties and use electronic structure analysis to reveal the origins of this disparity.

Our DFT adsorption energies, E_{ads} , show that Pb(II) binds in excess of 4 times more strongly to hematite than to commensurate alumina of the same surface stoichiometry, (HO)₃–M–M–R. This unprecedented result indicates that surface composition is a key factor in understanding experimentally determined reactivity trends. Analysis of Pb/Fe₂O₃ PDOS reveals that the Fe d states can participate in Pb adsorption in two ways. In all of our optimized Pb/Fe₂O₃ structures, Pb–O covalent interactions are stabilized by the partially occupied Fe d-band relative to the Pb–O interactions in alumina. Second, in the most preferred Pb/Fe₂O₃ geometry (Fe2A on either H-bonded surface), we report an additional electronic interaction in which O p, Fe d, and Pb s and p states mix, resulting in a drastic adjustment in net Fe spin and notable difference in the surface Fe PDOS. This second interaction is not present at any other Pb(II) adsorption sites, indicating an inherently fortuitous balance between Pb–O, Pb–Fe, and Fe–O distances and relative orientations at the Fe2 site on the (0001) surface. This finding could be key to understanding why the reactivity of α -Fe₂O₃ (0001) is greater than that of α -Fe₂O₃ (1102) toward Pb(II).⁸ Characterization of Pb adsorption at hematite surfaces also aids in understanding the persistence of Pb in top soil.

Our results demonstrate the utility of electronic structure modeling to study and extract fundamental molecular level understanding about geochemical interfaces. Empirical models based on bond valence relationships can not be used to predict the underlying electronic interactions and spin-state effects that dictate reactivity trends reported here. Similar studies of Pb(II)/M₂O₃ (1102) are underway to further elucidate the origins of observed reactivity trends as functions of both composition and surface structure/orientation.

Acknowledgment. This work was supported by NSF Grants CBET-0404400 and CHE-0431425, and utilized the high-performance computational capabilities of the Arctic Region Supercomputing Center at the University of Alaska Fairbanks, and Helix Systems Biowulf cluster at the National Institutes of Health, Bethesda, MD. S.E.M. was supported by a National Research Council (NRC) Postdoctoral Fellowship.

References and Notes

- (1) <http://www.atsdr.cdc.gov>.
- (2) Brown, G. E., Jr.; Foster, A. L.; Ostergren, J. D. *Proc. Natl. Acad. Sci. U.S.A.* **1999**, *96*, 3388.
- (3) Ostergren, J.; Brown, G., Jr.; Parks, G.; Tingle, T. *Environ. Sci. Technol.* **1999**, *33*, 1627.
- (4) Hochella, M. F., Jr.; Lower, S.; Maurice, P. A.; Penn, R. L.; Sahai, N.; Sparks, D.; Twining, B. *Science* **2008**, *319*, 1631.
- (5) Sparks, D. *Elements* **2005**, *1*, 193.
- (6) Hiemstra, T.; Yong, H.; Van Riemsdijk, W. *Langmuir* **1999**, *15*, 5942.
- (7) Brown, G. E., Jr.; Henrich, V. E.; Casey, W.; Clark, D.; Eggleston, C.; Felmy, A.; Goodman, D.; Gratzel, M.; Maciel, G.; McCarthy, M.; Nealon, K. *Chem. Rev.* **1999**, *99*, 77.
- (8) Brown, G. E., Jr.; Trainor, T. and Chaka, A. In *Chemical bonding at surfaces and interfaces*; Nilsson, A., Pettersson, L., Nørskov, J., Eds.; Elsevier: Amsterdam, 2007; pp 547–509.
- (9) Chambers, S. A.; Droubay, T.; Jennison, D.; Mattsson, T. *Science* **2002**, *297*, 827.

- (10) Niu, C.; Shepherd, K.; Martini, D.; Tong, J.; Kelber, J.; Jennison, D.; Bogicevic, A. *Surf. Sci.* **2000**, *465*, 163.
- (11) Henderson, M. *Surf. Sci. Rep.* **2002**, *46*, 5.
- (12) Kasprzyk-Hordern, B. *Adv. Colloid Interface Sci.* **2002**, *110*, 19.
- (13) Lo, C. S.; Tanwar, K. S.; Chaka, A. M.; Trainor, T. P. *Phys. Rev. B* **2007**, *75*, 075425.
- (14) Manceau, A.; Boisset, M.-C.; Sarret, G.; Hazemann, J.-L.; Mench, M.; Cambier, P.; Prost, R. *Environ. Sci. Technol.* **1996**, *30*, 1540.
- (15) Martínez, C. E.; McBride, M. *Environ. Sci. Technol.* **1999**, *33*, 745.
- (16) Elzinga, E.; Peak, D.; Sparks, D. *Geochim. Cosmochim. Acta* **2001**, *65*, 2219.
- (17) Dong, D.; Nelson, Y.; Lion, L.; Shuler, M.; Ghiorse, W. *Water Res.* **2000**, *34*, 427.
- (18) Villalobos, M.; Trotz, M.; Leckie, J. *Environ. Sci. Technol.* **2001**, *35*, 3849.
- (19) Schwertmann, U. *Plant Soil* **1991**, *130*, 1.
- (20) Stipp, S.; Hansen, M.; Kristensen, R.; Hochella, M.; Bennedsen, L.; Dideriksen, K.; Balic-Zunic, T.; Leonard, D.; Mathieu, H. *Chem. Geol.* **2002**, *190*, 321.
- (21) Sposito, G. *Chimia* **1989**, *43*, 169.
- (22) Stumm, W.; Morgan, J. *Aquatic Chemistry*; Wiley: New York, 1996.
- (23) Brown, G. E., Jr.; Parks, G. *Int. Geol. Rev.* **2001**, *43*, 963.
- (24) Brown, G. E., Jr.; Sturchio, N. *Appl. Synchrotron Radiat. Low-Temp. Geochem. Environ. Sci.* **2002**, *49*, 1.
- (25) Schindler, P. In *Adsorption of Inorganics at Solid-Liquid Interfaces*; Anderson, M., Rubin, A., Eds.; Ann Arbor Science Publishers, Inc.: Ann Arbor, MI, 1981; pp 1–49.
- (26) Hayes K.; Katz, L. In *Physics and Chemistry of Mineral Surfaces*; Brady, P., Ed.; CRC Press: Boca Raton, FL, 1996; pp 147–223.
- (27) Dzombak, D. A. and Morel, F., *Surface Complexation Modeling: Hydrous Ferric Oxide* (John Wiley and Sons, New York, 1990).
- (28) Bargar, J. R.; Brown, G. E., Jr.; Parks, G. A. *Geochim. Cosmochim. Acta* **1997**, *61*, 2639.
- (29) Ostergren, J.; Trainor, T.; Bargar, J.; Brown, G., Jr.; Parks, G. J. *Colloid Interface Sci.* **2000**, *225*, 466.
- (30) Bargar, J. R.; Brown, G. E., Jr.; Parks, G. A. *Geochim. Cosmochim. Acta* **1997**, *61*, 2617.
- (31) Bargar, J. R.; Towle, S. N.; Brown, G. E., Jr.; Parks, G. A. *Geochim. Cosmochim. Acta* **1996**, *61*, 3541.
- (32) Bargar, J. R.; Trainor, T. P.; Fitts, J. P.; Chambers, S. A.; Brown, G. E., Jr. *Langmuir* **2004**, *20*, 1667.
- (33) Trainor, T.; Templeton, A.; Parks, G. B. G. *Langmuir* **2002**, *18*, 5782.
- (34) Templeton, A. S.; Trainor, T. P.; Traina, S. J.; Spormann, A. M.; Brown, G. E., Jr. *Proc. Natl. Acad. Sci. U.S.A.* **2001**, *98*, 11897.
- (35) Yoon, T.; Trainor, T.; Eng, P.; Bargar, J.; Brown, G., Jr. *Langmuir* **2005**, *21*, 4503.
- (36) Bargar, J. R.; Towle, S. N.; Brown, G. E., Jr.; Parks, G. A. *J. Colloid Interface Sci.* **1997**, *185*, 473.
- (37) Liu, P.; Kendelewicz, T.; Brown, G. E., Jr.; Nelson, E. J.; Chambers, S. A. *Surf. Sci.* **1998**, *417*, 53.
- (38) Reference deleted in revision.
- (39) Zhang, L.; Tian, C.; Waychunas, G.; Shen, R. *J. Am. Chem. Soc.* **2008**, *130*, 7686.
- (40) Yin, S.; Ma, X.; Ellis, D. E. *Surf. Sci.* **2007**, *601*, 2426.
- (41) Zarzycki, P. *Appl. Surf. Sci.* **2007**, *253*, 7604.
- (42) Chambers, S. A.; Yi, S. *Surf. Sci.* **1999**, *439*, L785.
- (43) Thevuthasan, S.; Kim, Y.; Yi, S.; Chambers, S.; Morais, J.; Denecke, R.; Fadley, C.; Liu, P.; Kendelewicz, T.; Brown, G., Jr. *Surf. Sci.* **1999**, *425*, 276.
- (44) Wang, X. G.; Weiss, W.; Shaikhutdinov, S. K.; Ritter, M.; Petersen, M.; Wagner, F.; Schlogl, R.; Scheffler, M. *Phys. Rev. Lett.* **1998**, *81*, 1038.
- (45) Wasserman, E.; Rustad, J.; Felmy, A.; Hay, B.; Halley, J. *Surf. Sci.* **1997**, *385*, 217.
- (46) Ruberto, C.; Yourdshahyan, Y.; Lundqvist, B. I. *Phys. Rev. B* **2003**, *67*, 195412.
- (47) Verdozzi, C.; Jennison, D. R.; Schultz, P. A.; Sears, M. P. *Phys. Rev. Lett.* **1999**, *82*, 799.
- (48) Wang, X.-G.; Chaka, A.; Scheffler, M. *Phys. Rev. Lett.* **2000**, *84*, 3650.
- (49) Hass, K. C.; Schneider, W. F.; Curioni, A.; Andreoni, W. *Science* **1998**, *282*, 265.
- (50) Hass, K. C.; Schneider, W. F.; Curioni, A.; Andreoni, W. *J. Phys. Chem. B* **2000**, *104*, 5527.
- (51) Godin, T.; Lafemina, J. *Phys. Rev. B* **1994**, *49*, 7691.
- (52) Manassidis, I.; Devita, A.; Gillan, M. *Surf. Sci.* **1993**, *285*, L517.
- (53) Guenard, P.; Renaud, G.; Barbier, A.; Gautier-Soyer, M. *Surf. Rev. Lett.* **1998**, *5*, 321.
- (54) Walters, C.; McCarty, K.; Soares, E.; Van Hove, M. *Surf. Sci.* **2000**, *464*, L732.
- (55) Toofan, J.; Watson, P. R. *Surf. Sci.* **1998**, *401*, 162.
- (56) Noguera, C. *J. Phys.-Condensed Matter* **2000**, *31*, R367.
- (57) Ketteler, G.; Weiss, W.; Ranke, W. *Surf. Rev. Lett.* **2001**, *8*, 661.
- (58) Shaikhutdinov, S.; Weiss, W. *Surf. Sci.* **1999**, *432*, L627.
- (59) Lemire, C.; Bertarione, S.; Zecchina, A.; Scarano, D.; Chaka, A. M.; Shaikhutdinov, S.; Freund, H.-J. *Phys. Rev. Lett.* **2005**, *94*, 166101–1.
- (60) Barbier, A.; Stierle, A.; Kasper, N.; Buittet, M.-J.; Jupille, J. *Phys. Rev. B* **2007**, *75*, 233406.
- (61) Jarvis, E. A. A.; Chaka, A. M. *Surf. Sci.* **2007**, *601*, 1909.
- (62) Bergermayer, W.; Schweiger, H.; Wimmer, E. *Phys. Rev. B* **2004**, *69*, 195409.
- (63) Rohrbach, A.; Hafner, J.; Kresse, G. *Phys. Rev. B* **2004**, *70*, 125426.
- (64) Reuter, K.; Scheffler, M. *Phys. Rev. B* **2002**, *65*, 035406.
- (65) Sun, Q.; Reuter, K.; Scheffler, M. *Phys. Rev. B* **2003**, *67*, 205424.
- (66) Eggleston, C. M.; Stack, A. G.; Rosso, K. M.; Higgins, S. R.; Bice, A. M.; Boese, S. W.; Pribul, E. D.; Nichols, J. J. *Geochim. Cosmochim. Acta* **2003**, *67*, 985.
- (67) Becker, U.; Hochella, M.; Apra, E. *Am. Mineral.* **1995**, *81*, 1301.
- (68) Venema, P.; Hiemstra, T.; Weidler, P.; van Riemsdijk, W. *J. Colloid Interface Sci.* **1998**, *198*, 282.
- (69) Trainor, T. P.; Chaka, A. M.; Eng, P. J.; Newville, M.; Waychunas, G. A.; Catalano, J. G.; Brown, G. E., Jr. *Surf. Sci.* **2004**, *573*, 204.
- (70) Eng, P. J.; Trainor, T. P.; Brown, G., Jr.; Waychunas, G. A.; Newville, M.; Sutton, S. R.; Rivers, M. L. *Science* **2000**, *288*, 1029.
- (71) Meyer, R.; Ge, Q.; Lockmeyer, J.; Yeates, R.; Lemanski, M.; Reinalda, D.; Neurock, M. *Surf. Sci.* **2007**, *601*, 134.
- (72) Hinnemann, B.; Carter, E. A. *J. Phys. Chem. C* **2007**, *111*, 7105.
- (73) Rollmann, G.; Rohrbach, A.; Entel, P.; Hafner, J. *Phys. Rev. B* **2004**, *69*, 165107.
- (74) Perdew, J. P.; Burke, K.; Ernzerhof, M. *Phys. Rev. Lett.* **1996**, *77*, 3865.
- (75) Delley, B. *J. Chem. Phys.* **1990**, *92*, 508.
- (76) Delley, B. *J. Chem. Phys.* **2000**, *18*, 7756.
- (77) Monkhorst, H. J.; Pack, J. D. *Phys. Rev. B* **1976**, *13*, 5188.
- (78) *Crystal Structures*; John Wiley and Sons: New York, 1964; Vol. 2.
- (79) Finger, L. W.; Hazen, R. M. *J. Appl. Phys.* **1980**, *51*, 5362.
- (80) Lide, D. R., Ed.; *CRC Handbook of Chemistry and Physics*, 85th ed.; CRC Press: Boca Raton, FL, 2004.
- (81) Leciejewicz, J. *Acta Crystallogr.* **1961**, *14*, 1304.
- (82) Harada, H.; Sasa, Y.; Uda, M. *J. Appl. Crystallogr.* **1981**, *14*, 141.
- (83) Perdew, J. P.; Wang, Y. *Phys. Rev. B* **1992**, *45*, 13244.
- (84) Delley, B. *Int. J. Quantum Chem.* **1998**, *69*, 423.
- (85) Delley, B. *Phys. Rev. B* **2002**, *65*, 155125.
- (86) Benjelloun, A.; Daoudi, A.; Chermette, H. *J. Chem. Phys.* **2005**, *122*, 154304.
- (87) Benjelloun, A.; Daoudi, A.; Chermette, H. *J. Chem. Phys.* **2004**, *121*, 7207.
- (88) Benjelloun, A.; Daoudi, A.; Chermette, H. *Mol. Phys.* **2005**, *103*, 317.
- (89) Walsh, A.; Watson, G. W. *J. Solid State Chem.* **2005**, *178*, 1422.
- (90) Payne, D.; Egdell, R. G.; Law, D.; Glans, P. A.; Learmonth, T.; Guo, K. E. S. J.; Walsh, A.; Watson, G. W. *Phys. Rev. Lett.* **2006**, *96*, 157403.
- (91) Brown, I.; Shannon, R. *Acta Cryst. A* **1973**, *29*, 266.
- (92) Hoffman, R. *Rev. Mod. Phys.* **1988**, *60*, 601.
- (93) Lodziano, Z.; Nørshov, J. K.; Stoltze, P. *J. Chem. Phys.* **2003**, *118*, 11179.
- (94) Felice, R. D.; Northrup, J. E. *Phys. Rev. B* **1999**, *60*, 16287R.
- (95) Payne, D.; Egdell, R. G.; Walsh, A.; Watson, G. W.; Guo, J.; Glans, P. A.; Learmonth, T.; Smith, K. E. *Phys. Rev. Lett.* **2006**, *96*, 157403.
- (96) Certain commercial software is identified in this paper to foster understanding. Such identification does not imply recommendation or endorsement by the National Institute of Standards and Technology, nor does it imply that the software identified is necessarily the best available for the purpose.
- (97) For each oxide, we observe no appreciable differences in PDOS on the 1D2U and 2D1U surfaces, and report only the former here.
- (98) ρ_d for our large periodic systems as computed in DMol³ are necessarily computed without converged k -point sampling, and on a sparse numerical grid. The resulting visualization is qualitatively useful in understanding Pb sorption, but is not adequate for quantitative measurement of electronic properties.